Chapter 5

Flows in Quiescent Coronal Loops

In this chapter, we observed quiescent coronal loops using multi-wavelength observations from the Atmospheric Imaging Assembly (AIA) aboard the Solar Dynamics Observatory (SDO) on 13 April 2016. The flows at the foot points of such loop systems are studied using spectral data from the Interface Region Imaging Spectrograph (IRIS). The Doppler velocity distributions at the foot points lying in the moss region show the negligible or small flows at the Ni I, Mg II k3, and C II line corresponding to upper photospheric and chromospheric emissions. Significant red shifts (downflows) ranging from 1 to 7 km s^{-1} are observed at Si IV (1393.78 Å ; log(T/K)=4.8), which is found to be consistent with the existing results regarding dynamical loop systems and moss regions. Such downflows agree well with the impulsive heating mechanism reported earlier. This work is published in "Annales Geophysicae" Journal.

Yamini K. Rao, Abhishek K. Srivastava, Pradeep Kayshap, and Bhola N. Dwivedi, *Ann. Geophys., 37, 765–773, (2019)*

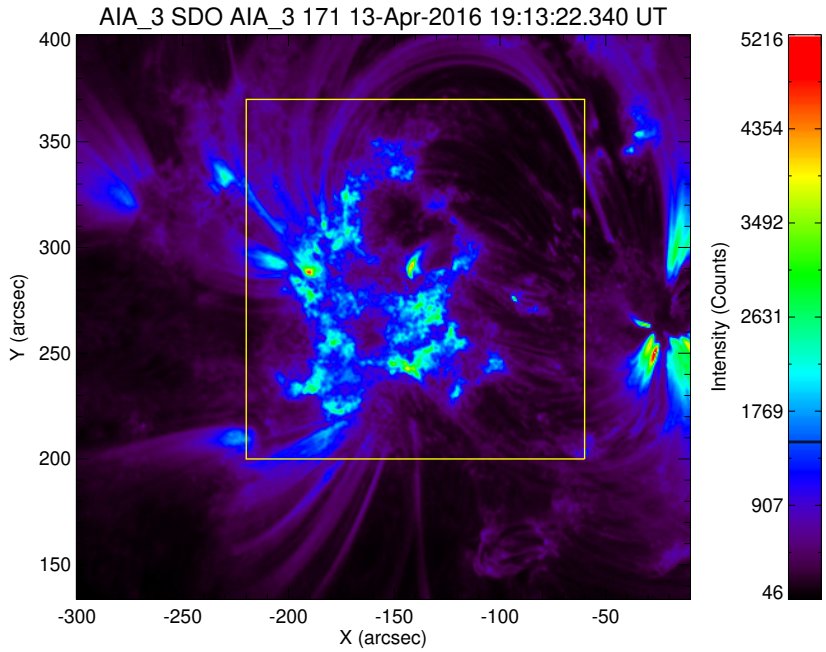

Figure 5.1: Intensity emission due to 171 Å wavelength of SDO/AIA at 19:13:22 UT. The yellow box is overlaid to show the region of interest (ROI) taken to analyse the flows at the footpoints of quiescent coronal loops.

5.1 Introduction

The active regions dominated by various loop structures are of significant importance for the study of coronal heating, since these loop systems act as a fundamental unit of the solar corona (De Moortel & Browning, 2015; Klimchuk, 2006; Reale, 2014). Moss is generally associated with plage regions around the active regions sites (Fletcher & De Pontieu, 1999), and transition region emission of hot core loops will provide us with a better understanding of the flows and thus energy transfer mechanism between the TR and corona.

Klimchuk (2006) provided a full review of the coronal heating problem. It describes how the coronal heating mechanisms are impulsive when explored from the perspective of elemental magnetic flux strands. It has also been well established that the loop structures emit significantly in the solar corona, which has been classified depending on their temperatures. The spectral studies of these loop systems in response to the Doppler shift provide

a clue for distinguishing between the steady and impulsive heating mechanism (Brooks et al., 2011; Del Zanna, 2008).

Various types of loops are hot core loops (Del Zanna, 2008), warm loops (Del Zanna et al., 2011), fan loops (Warren & Brooks, 2009; Young et al., 2012, and references therein) and cool loops (Huang et al., 2015; Rao et al., 2019) present in the different regions of the solar atmosphere. The temperature and density diagnostics of quiescent coronal loops have been fairly studied earlier (Del Zanna & Mason, 2003). However, there have been not many observations regarding the flows in the resolved strands/flux tubes of such loops in the solar corona.

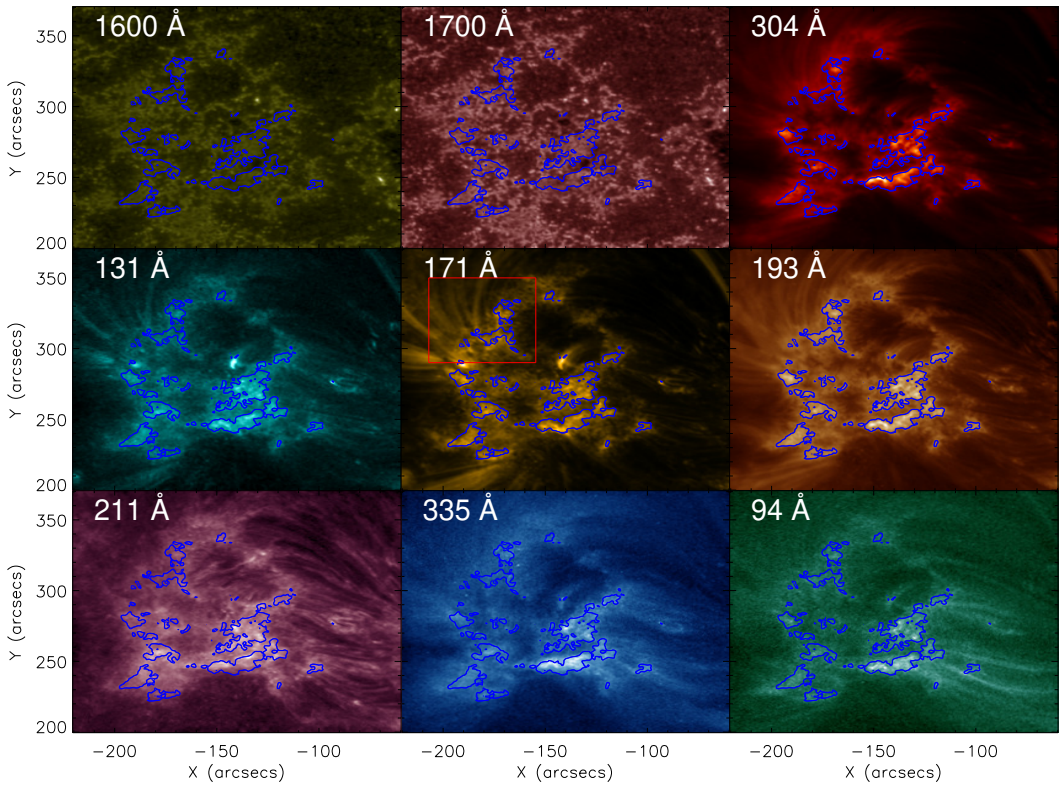

Figure 5.2: Mosaic representation of the zoom-in-view of the region of interest at different wavelength of SDO/AIA as mentioned on the corresponding panels.

In this chapter, we study quiescent coronal loops with big loop arches having one of their footpoints anchored at the edges of moss region. The different strands in such large loop systems were identified using high-resolution observations of SDO/AIA, and the

flows in it were studied, mapping the footpoints to the lower region of the solar atmosphere. Sect. 5.2 describes the observational data and its analyses presenting the details of the data used for our analyses. In Sect. 5.3, the results have been reported with their interpretations. In the last section, the discussion and conclusions are summarized.

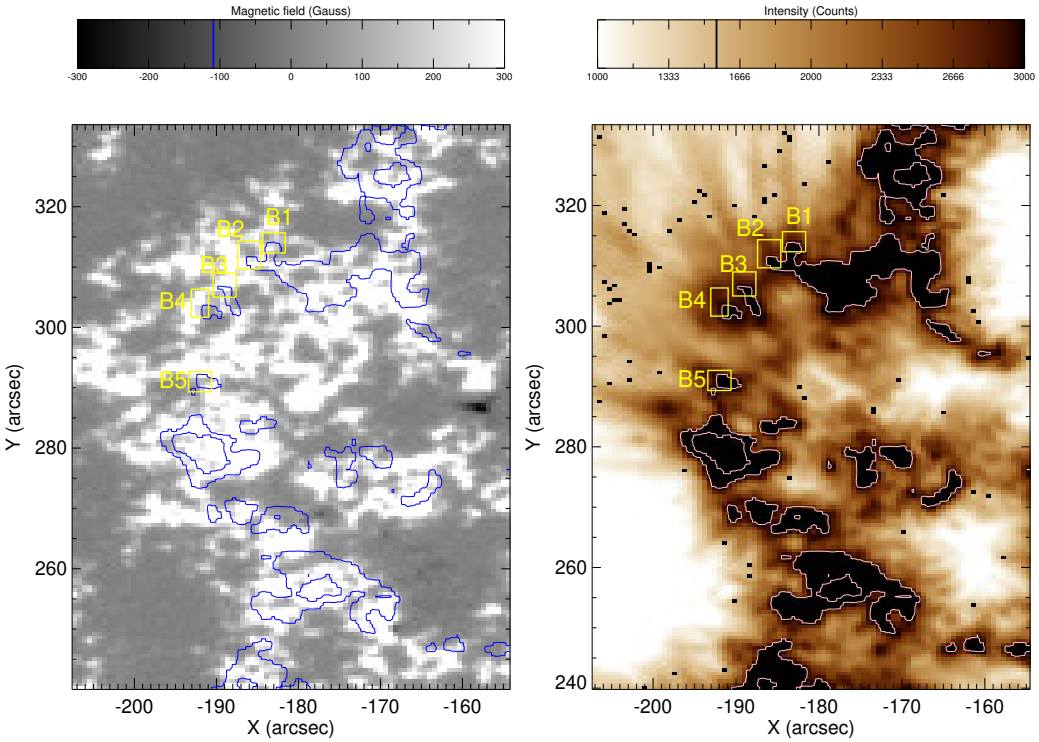

Figure 5.3: Left panel: HMI map indicating the magnetic polarities at the moss region indicted by blue contours. Right panel: Identification of the footpoints of quiescent loops anchored at the moss regions. The different small boxes are taken at the footpoints of the individual loop strands are shown in both the panels.

5.2 Observational Data

IRIS provides spectral data in the two UV domains: FUV band (1331.7 Å to 1358.4 Å and 1389.0 Å to 1407.0 Å) and NUV domain (2782.7 Å to 2835.1 Å), with a large number of spectral lines covering the photosphere, chromosphere, TR, and inner corona. Level 2 data are used for our study which are calibrated for the dark current removal, flat fielding

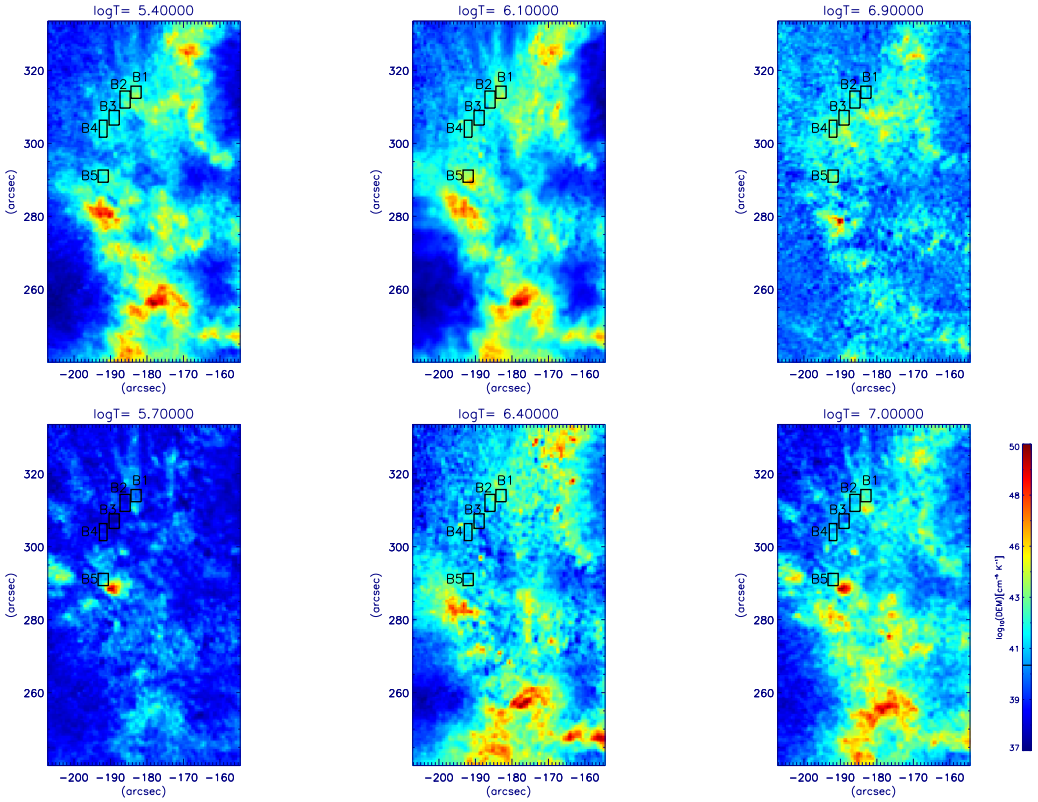

Figure 5.4: Differential Emission Measure maps of the plage region contaning the moss associated to footoints of quiescent coronal loop systems.

effect (De Pontieu et al., 2014a). We utilized Si IV (1393.78 Å), Mg II k (2796.20 Å), C II (1334.53 Å), and Ni I (2799.47 Å) spectral lines.

In this work, we used dense raster data from IRIS for the time period 19:19:09 to 20:21:14 UTC on 13th April 2016 targeting the evolution of AR 12529 having slit width of 0.35" having step cadence of 9.3 s covering the field-of-view of 141" in x-direction and 175" in y-direction centered at the coordinates (X_{cen}, Y_{cen}) = (−173", 275"). The data are compensated for oscillations due to thermal variation using iris_orbitvarr_corr_l2.pro in the SSWIDL library. The rest wavelengths for different spectral lines used in our analysis are calibrated using neutral lines from the relatively quiet-Sun area of the raster. The rest wavelength of Ni I used is 2944.4697 Å. Mg II k has been calibrated with respect to Ni I which is found to be 2796.3574 Å. Si IV line is calibrated w.r.t Fe I (1392.8052 Å) line

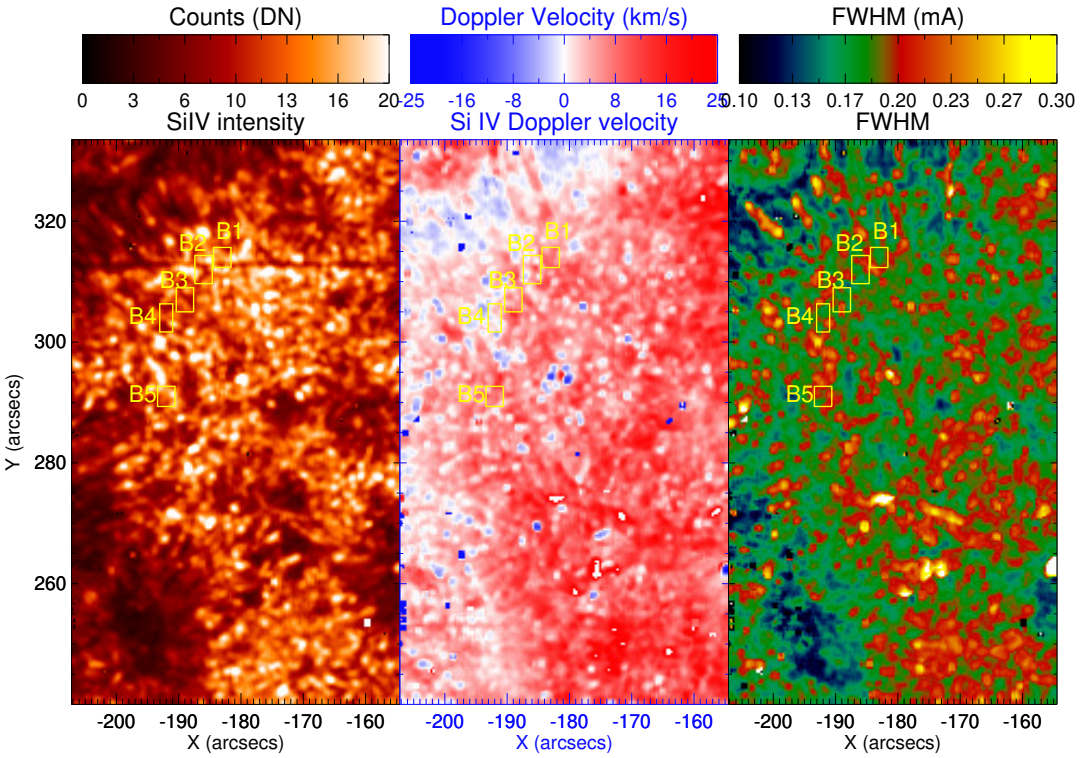

Figure 5.5: The different parametric plots of Si IV (1393.78 Å) line with the footpoints of the quiescent coronal loop systems indicated by different boxes.

and C II is calibrated w.r.t O I (1355.5987 Å). Thus, the calibrated wavelengths used for our analysis is 1393.7604 Å and 1334.5406 Å for Si IV and C II respectively.

The Doppler velocities are deduced using different spectral lines, i.e., Ni I 2799.47 Å, Mg II k 2796.20 Å, C II 1334.53 Å, and Si IV 1393.78 Å respectively associated with the formation temperature of log(T/K) = 4.2, 4.0, 4.3, and 4.8. The velocity resolution of IRIS is 1 km s^{-1} (De Pontieu et al., 2014a).

Si IV shows the characteristics of optically thin line and is thus fitted with the single Gaussian curve while Ni I is absorption line and the inverse Gaussian curve is fitted. Mg II k and C II are fitted with single or double Gaussian depending on their profile characteristics.

The corresponding SDO/AIA observations are also taken in the different filters covering UV/EUV range corresponding to a different temperature range in the solar atmosphere.

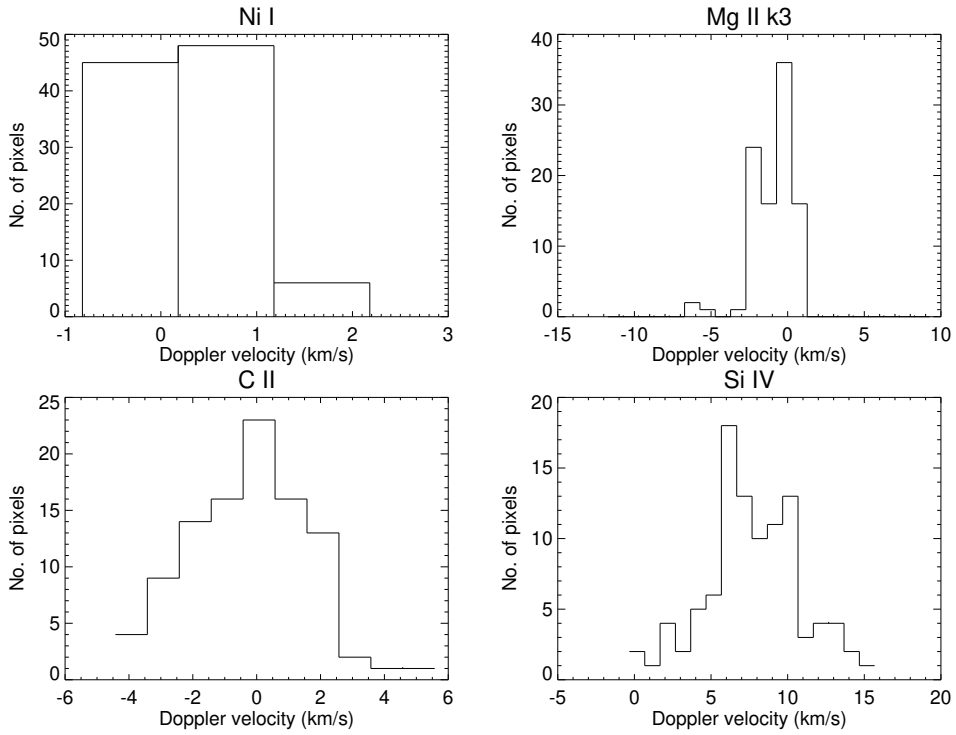

Figure 5.6: The velocity distributions for different spectral lines corresponding to different temperatures at box B1.

AIA provides full-disk multi-wavelength observations of coronal lines having a spatial resolution of 1.5" with a pixel size of 0.6", and temporal cadence of 12 s (Lemen et al., 2012).

The co-aligned Level 2 SDO/AIA data cube was used in which all the wavelengths are matched to the field of view of 1600 Å. To co-align with the raster images of Si IV (1393.78Å), the near-time 171 Å image properly cross-correlated with 1600 Å was used to compensate for the different resolution of two instruments. However, in our work, we study the bulk plasma flows from the chosen moss region (in various boxes) by deducing the integrated spectral line-profiles of various IRIS lines. The plage regions are identified in SDO/AIA image data, and the location is mapped onto comparatively high-resolution IRIS data.

5.3 Observational Results

Fig. 5.1 shows the intensity emission of AR 12529, where the plage region and various loops anchored in the moss region are visible in 171 Å wavelength of SDO/AIA. The green emission predominantly indicates the highest emission representing the part of the moss region. The yellow box is overlaid to show the region of interest (ROI).

In Fig. 5.2, the moss region has been identified with the brightest emission in SDO/AIA 193 Å filter. The intensity threshold of above 3000 counts (see Fig. 5.1), with values double those of plage region surrounding it has been set which is shown by contours overlying on the different filters corresponding to different temperature ranges from the upper photosphere to corona. The northern segment of the moss regions where the quiescent coronal loops are anchored was further taken to analyse the flows at the footpoints of these loop systems. The different bands of AIA show different morphological characteristics of an AR. 1600 Å and 1700 Å represent the continuum emission at the upper photosphere showing plage region near the active region, and 304 Å yields the chromospheric emission of the plage region. The hot loop structures are not distinctly visible. The middle row shows the inner coronal channels where quiescent coronal loops are clearly visible, and moss region is identified. The last row shows the hot channels of SDO/AIA (335 Å, 211Å, and 94 Å) where the quiescent loops taken for our analysis are not visible since quiescent loops are dominated by emissions from the temperatures ranging from 0.7 to 1 MK corresponding to SDO/AIA filters.

The left panel of Fig. 5.3 shows the HMI map of the region of interest (ROI) indicating the magnetic polarities at the moss region as well as footpoints of the quiescent coronal loops are shown. The right panel of Fig. 5.3 is the emission of 193 Å line plotted in reverse color to identify the footpoints. The different boxes of different sizes are then chosen around the footpoints to cover the full strand of loop.

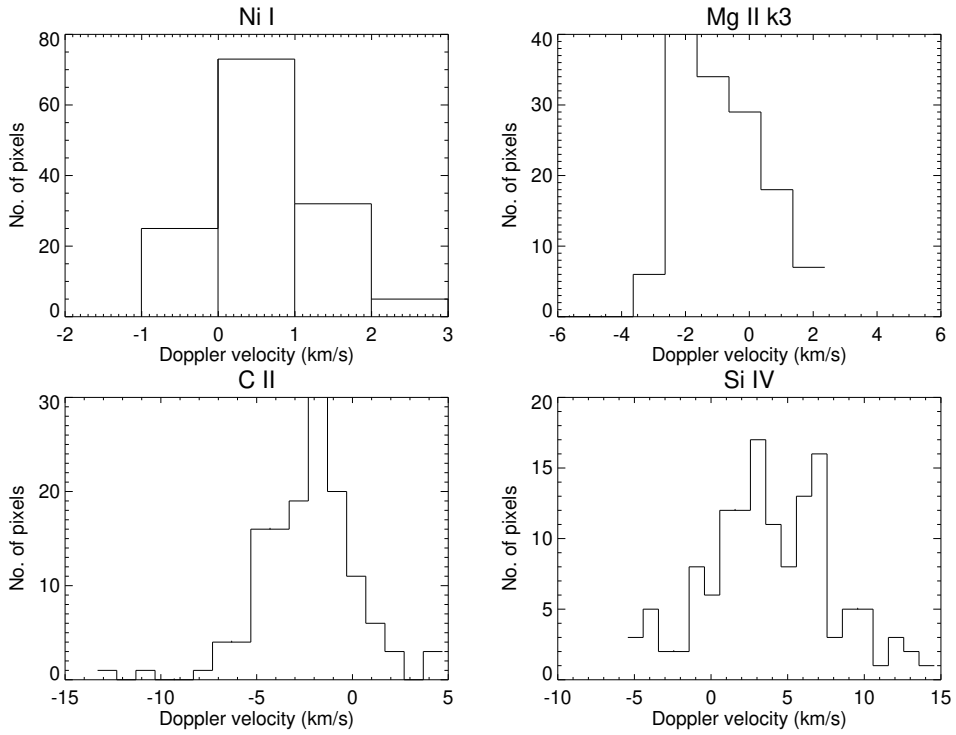

Figure 5.7: The velocity distributions for different spectral lines corresponding to different temperatures at box B2.

Fig. 5.4 shows the DEM maps of the ROI derived by using automated method discussed by Hannah & Kontar (2012) in which plasma emission at different temperatures has been shown. The colorbar indicates the range of the DEM values. These maps shows the presence of multi-thermal plasma at the footpoints of the quiescent coronal loop systems shown by the boxes around it.

Fig. 5.5 shows the parametric plots of the Si IV (1393.7604 Å) showing the intensity, Doppler velocity, and FWHM maps where the values has been indicated by the colorbars over the plots. The Doppler velocity maps shows that the TR is dominated by red-shifts even in the plage region surrounding the moss in which footpoints have been taken for our analysis.

The Doppler velocity distribution is thus explored at different locations labelled as B1, B2, B3, B4, and B5. Positive values (redshifts) represent downflows, while the negative values (blueshifts) indicate upflows. The Doppler velocity at each pixel in first box (B1) for

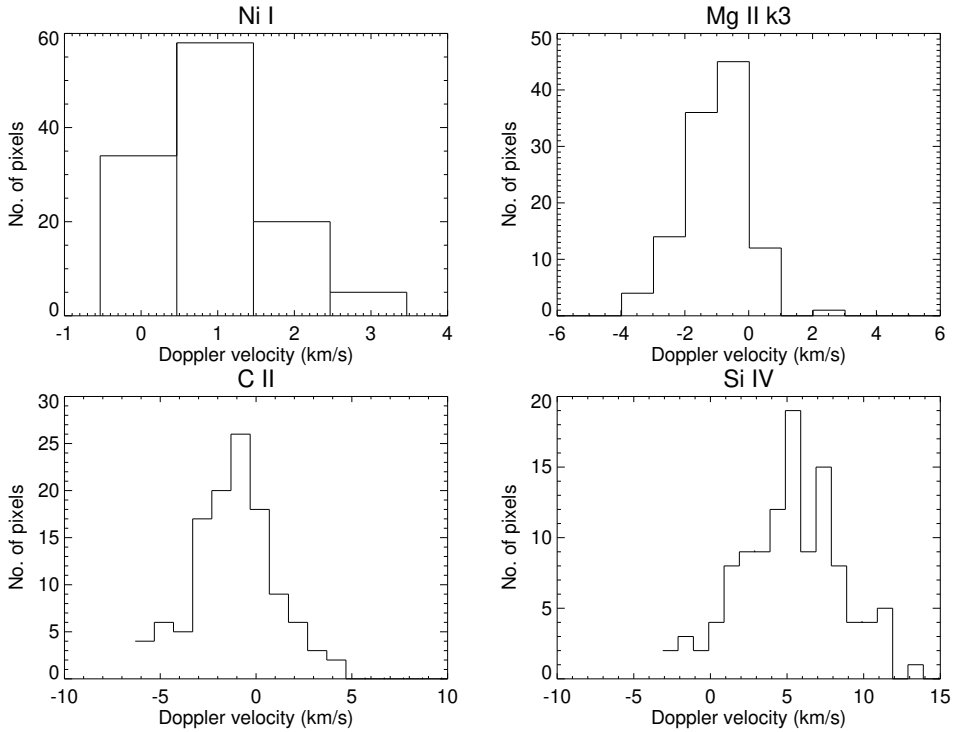

Figure 5.8: The velocity distributions for different spectral lines corresponding to different temperatures at box B3.

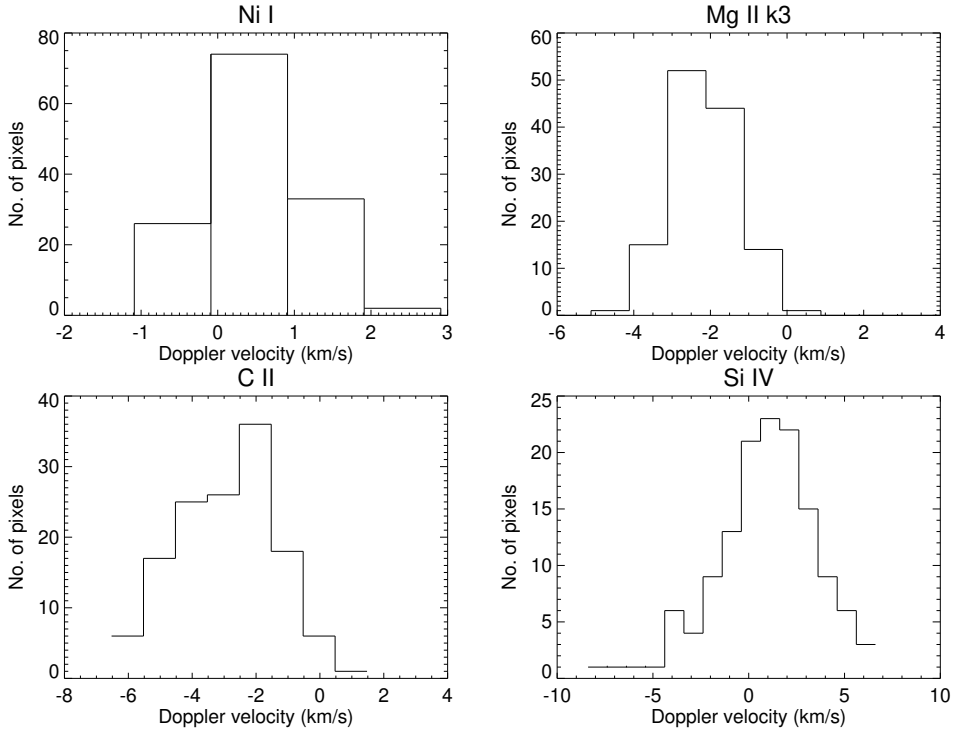

Figure 5.9: The velocity distributions for different spectral lines corresponding to different temperatures at box B4.

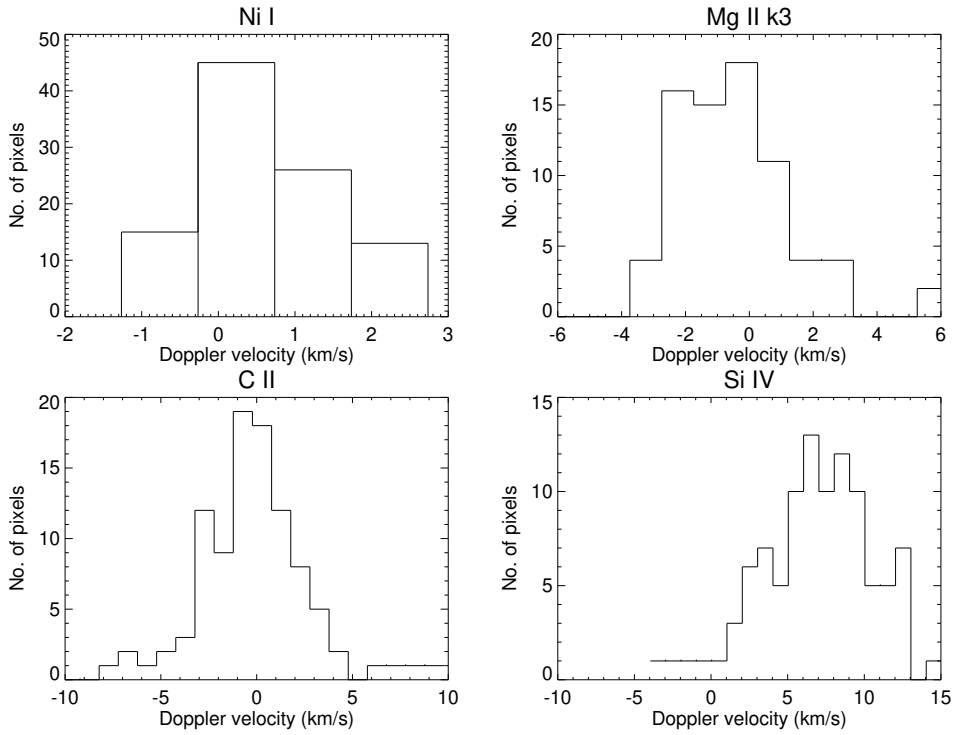

Figure 5.10: The velocity distributions for different spectral lines corresponding to different temperatures at box B5.

different spectral lines is then shown Fig. 5.6. The velocity distribution for Ni I shows the spread around 0 km s^{-1} ranging from $(-0.8$ to $+2.2)$ km s^{-1} . Mg II k shows the velocities ranging from $(-5$ to $+1)$ km s^{-1}, while C II has $(-5$ to $+5)$ km s^{-1} . Si IV shows redshifts having Doppler velocities ranging from (0 to $+15$) km s^{-1} . The histogram of the Doppler velocity for different spectral lines indicate the redshifts in the Si IV line and very small or negligible flows at Ni I, Mg II k, and C II.

Similarly, such Doppler velocity distribution is shown in Fig. 5.7, Fig. 5.8, Fig. 5.9, and Fig. 5.10 for different boxes labelled as B2, B3, B4, and B5.

Fig. 5.11 shows the average Doppler shift of different spectral lines as a function of their temperatures for different boxes chosen at the footpoints of the loops. Ni I (2799.47 Å) corresponds to upper photosphere, Mg II k yields emission ranging from mid-chromosphere to upper chromosphere. The core defined by (k3) forms little higher

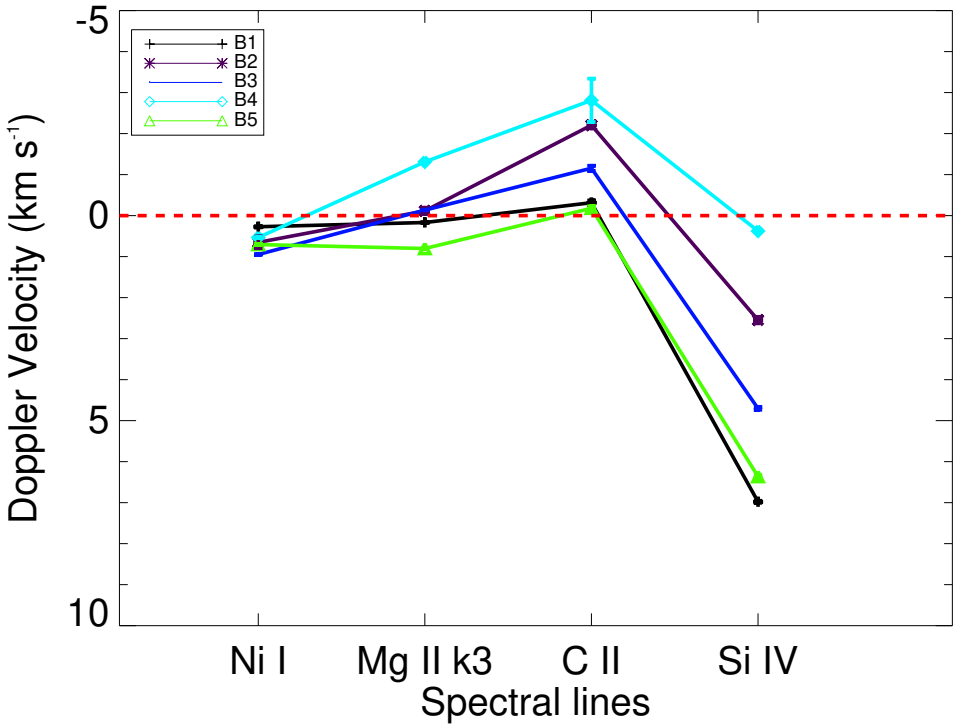

Figure 5.11: Average Doppler velocity variations for different spectral lines dominating at different heights in the solar atmosphere for boxes B1, B2, B3, B4, and B5 at the footpoints of quiescent coronal loops.

than the wings at 200 km below TR (Leenaarts et al., 2013). The C II core gives emission from 2.1 Mm, while Si IV corresponds to the TR emission (Rathore et al., 2015).

The Doppler velocity of the Ni I line has negligible values, indicating almost no flows (0.27 to 0.70) km s^{-1}, corresponding to the photospheric region. The blueshifts (upflows) show small increment for B2, B4, and B4 (-0.11 to -0.31) km s^{-1}, while they remain almost same for B1 (0.16 km s^{-1}) and B5 (0.80 km s^{-1}) up to the formation temperature of Mg II k. The C II line shows considerable blueshifts (upflows) (-0.17 to -2.81) km s^{-1} but it is still negligible as compared to chromospheric flows. The Doppler velocity variation at Si IV shows prevalent redshifts (downflows) at all the locations corresponding to TR flows (0.37 to 6.97) km s^{-1}. The 1-σ error is shown as error bars which is difficult to visualize in Fig. 5.11 owing to its very small values.

5.4 Discussion and Conclusions

The co-spatial multi-spectral Doppler velocity trend at the footpoints of quiescent coronal loops was studied. The Doppler velocity variation shows small flows (upflows/downflows) for Ni I and Mg II k the photospheric as well as the chromospheric region. C II shows very blueshifts (-0.1 to -2.81) km s^{-1} indicating small upflows at upper chromospheric region. The Doppler velocities then change to redshifts at the formation temperature of Si IV line, corresponding to the TR.

It was previously shown that the moss regions show significant redshifts (downflows) in the TR, explaining the low-frequency heating (Bradshaw & Cargill, 2010). The high- and low- frequency mechanisms depend upon the time taken by the loops to cool down as compared to heating frequency (Tripathi et al., 2008).

Our study of the flows at the quiescent coronal loops shows similar characteristics as the dynamically active loops, though the velocity values are smaller. The plasma predominantly shows redshifts at TR temperatures which corroborate with the low-frequency heating of loops in the coronal part of the solar atmosphere. These observations thus agree with the coronal loops heated up by low-frequency nanoflares via impulsive heating mechanism. Also, Patsourakos & Klimchuk (2006) observed the symmetric profiles for steady heating in the loops. Though it is possible to have asymmetries in the individual profile for which velocity distribution has been observed, our speculation supports the nano-flare driven impulsive heating mechanism for the quiescent coronal loops.

The asymmetries may also cause these Doppler variation in the spectral profiles due to a difference in the pressures (Mariska & Boris, 1983). So, other possibilities cannot be ruled out.